NJC

ROYAL SOCIETY OF CHEMISTRY

PAPER

View Article Online
View Journal | View Issue

Cite this: *New J. Chem.*, 2025, **49**, 2129

Influence of water-in-salt electrolytes on the electrochemical performance of porous N and S co-doped carbon electrodes in supercapacitors

S. Thior,[a] V. N. Kitenge,[a] Kabir O. Otun,[a] Rashed A. M. Adam,[a] Ndeye F. Diop,[a] Balla D. Ngom[b] and N. Manyala *[a]

This study demonstrates the impact of water-in-salt (WIS) electrolytes on the performance of a supercapacitor using nitrogen and sulphur co-doped activated carbon as the electrode material, highlighting its potential for enhanced energy storage capabilities. The electrolyte (WIS) used is 12 m $NaNO_3$ and the electrode material is a previously reported nitrogen and sulphur co-doped activated carbon sourced from mangosteen shells (NS-MSAC). Furthermore, the three-electrode test of NS-MSAC demonstrates a high specific capacitance of 206 F g^{-1} at a current density of 0.5 A g^{-1} within a potential window of 0 to −1.0 V. The symmetric supercapacitor built with NS-MSAC achieved a voltage range of 0–2.0 V by exploiting the beneficial electrochemical properties of 12 m $NaNO_3$, which include a higher potential window, low viscosity, high conductivity, and electrochemical stability. The assembled symmetric device featuring NS-MSAC//NS-MSAC delivered a specific energy of 25 W h kg^{-1} at a power density of 512 W kg^{-1}. Additionally, after 8000 charge/discharge cycles, approximately 85% of the capacitance was retained. This highly concentrated aqueous electrolyte strategy is promising for achieving remarkable supercapacitor performance.

Received 16th October 2024,
Accepted 27th December 2024

DOI: 10.1039/d4nj04507f

rsc.li/njc

1. Introduction

Supercapacitors have garnered consistent research interest due to their exceptional features, including rapid charge/discharge capabilities, high specific power ($P_D \sim 10^5$ W kg^{-1}), electrochemical stability, and the potential to mitigate the limitations of batteries, such as low power density.[1] Supercapacitors are versatile energy storage devices with diverse applications in portable electronics, wearable technology, telecommunications, electric vehicles, and regenerative braking in the automotive industry.[2] Despite their widespread adoption, supercapacitors face a significant limitation such as their energy storage capacity (ED $<$ 10 W h kg^{-1}) that falls short compared to Li-ion batteries.[3] To overcome this constraint, researchers have been actively exploring innovative electrode materials and electrolytes, which are key factors for enhancing their specific energy.[4] Electrical double layer capacitors (EDLCs) are a class of supercapacitors in which energy is stored *via* ion adsorption at the surface of the electrode–electrolyte interface.[2] Carbon materials such as activated carbons (ACs), graphene, carbon nanotubes and carbon fibres are the major electrode materials that constitute EDLCs and are characterised by fascinating physicochemical properties including high surface area, high electrical conductivity, environmentally friendly nature, low cost, and the potential for excellent doping modifications.[5] The synthesis of ACs has garnered significant interest recently due to its potential for recycling biomass waste. These wastes serve as precursors for producing valuable ACs. Various types of biomasses have been explored, including banana peels, peanut shells, mangosteen shells, chicken bones, potato peels, pepper seeds, cocoa pods, and so on.[6–12] The pore size, surface area, and chemical composition of the AC material define its electrochemical characteristics.

Matching the pore size of activated carbon (AC) with the electrolyte can significantly influence the specific capacitance of electric double-layer capacitors (EDLCs).[13] Additionally, incorporating heteroatoms (such as nitrogen, oxygen, sulphur, and phosphorus) into AC[6] contributes to pseudo-capacitance, enhancing the performance by inducing electrical rearrangement in the carbon structures.[14] In this case, the carbon-based material exhibits EDLC behaviour, while the dopant atom leads to pseudocapacitive behaviour at the interface between the electrode and electrolyte.[15,16] Co-doping carbon with heteroatoms such as

[a] *Department of Physics, Institute of Applied Materials, SARChI Chair in Carbon Technology and Materials, University of Pretoria, Pretoria 0002, South Africa. E-mail: ncholu.manyala@up.ac.za*
[b] *Laboratoire de Photonique Quantique, d'Energie et de Nano-Fabrication, Faculté des Sciences et Techniques, Université Cheikh Anta Diop de Dakar (UCAD), B.P. 5005, Dakar-Fann Dakar, Senegal*

nitrogen and sulphur produces a variable electron density by establishing C–N and C–S type bonds. This combination incorporates active centres that display better hydrophilicity, high conductivity, and polarizability.[17] Additionally, heterostructure doping could provide significant contributions to wettability and electronic properties.[18]

To enhance the energy density of supercapacitors, both the capacitance (C) and the voltage (V) are critical factors. As per the energy density formula:

$$E = \frac{1}{2}CV^2, \quad (1)$$

the specific energy of supercapacitors is directly proportional to the square of the cell voltage. Since the potential window is directly related to the electrolyte, designing electrolytes that can achieve a high potential window will significantly increase the specific energy of SCs.[17,19] Among SC electrolytes, ionic liquids and organic electrolytes offer a large electrochemical stability window (2.5–4.0 V), boosting the energy density. However, they are costly, not so conductive, highly viscous, environmentally polluting, and pose safety risks. Aqueous electrolytes have several benefits over organic and ionic liquid electrolytes, such as superior safety operation, low cost, and high ionic conductivity.[20] On the other hand, the narrow potential window of water at 1.23 V severely limits the specific energy and their widespread applications.[21–23] Recently, water-in-salt (WIS) electrolytes have emerged as novel electrolytes for supercapacitors as they are capable of suppressing water decomposition, while delivering a high cell voltage and high specific energy. WIS electrolyte is an aqueous electrolyte with a high concentration solution where the salt outnumbers the solvent in both mass and volume.[24,25] In the solvation shell of water-in-salt (WIS) electrolytes, a high degree of electrochemical stability is achieved when water molecules coordinate with ions, thereby suppressing water splitting (approximately 1.2 V) at high potentials.[26] This coordination enables the expansion of the aqueous electrolyte voltage window beyond the water splitting limit (exceeding 2 V), beneficial to enhance the energy density in electrochemical energy storage systems. For instance, Hasegawa *et al.* prepared highly porous activated carbon from melamine and used an 18.7 m LiTFSI-based WIS electrolyte, leading to a device that delivered a potential window of 2.4 V and a specific energy of 24 W h kg^{-1} (ref. 27). David *et al.* investigated high-voltage WIS based on an 8 m NaTFSI electrolyte for supercapacitors. At a voltage of 1.8 V, the symmetrical device fabricated using activated carbon offered an enhanced specific energy of 14.4 W h kg^{-1}.[28]

To demonstrate the contribution of co-doped AC (high specific capacitance) and WIS (high potential window) in supercapacitors, this paper investigates the synergistic effects of utilizing a 12 m (m = mol kg^{-1}) $NaNO_3$ water-in-salt solution as the electrolyte in supercapacitor electrochemical measurements, with nitrogen and sulphur co-doped activated carbon serving as both positive and negative electrodes. The 12.0 m $NaNO_3$ electrolyte solution was selected due to its excellent properties including high solubility, high conductivity, and environmentally friendly nature. The electrochemical results show that this electrolyte demonstrated a wide electrochemical stability window of 2.0 V while benefiting from the high specific capacitance of the nitrogen and sulphur co-doped AC (NS-co-doped MS AC). The symmetric device designed by using NS-co-doped MS AC//NS-co-doped MS AC displays a superior energy density of 25 W h kg^{-1} with an equivalent specific power of 0.512 kW kg^{-1} at 0.5 A g^{-1}. Furthermore, the device achieved a remarkable coulombic efficiency of 99.6% and a capacitance retention of 85% after 8000 charge–discharge cycles at 5 A g^{-1}.

2. Experimental

The NS-MSAC and MSAC active materials were prepared using a one-step carbonization activation process, as previously reported.[29,30] Activated carbon was produced from mangosteen shells (M-S) using a one-step carbonization/activation technique (as depicted in Scheme 1).[29] For the NS MS AC, the mixture included 5 g mangosteen shell powder, 5 g K_2CO_3, and 1.25 g thiourea. Each mixture was combined with 5 mL deionized water to form cakes, dried at 60 °C for 12 hours, and then heated to 700 °C in a tube furnace under argon flow (200 cm^3 min^{-1}) for 2 hours. The products were separately immersed in 3 M

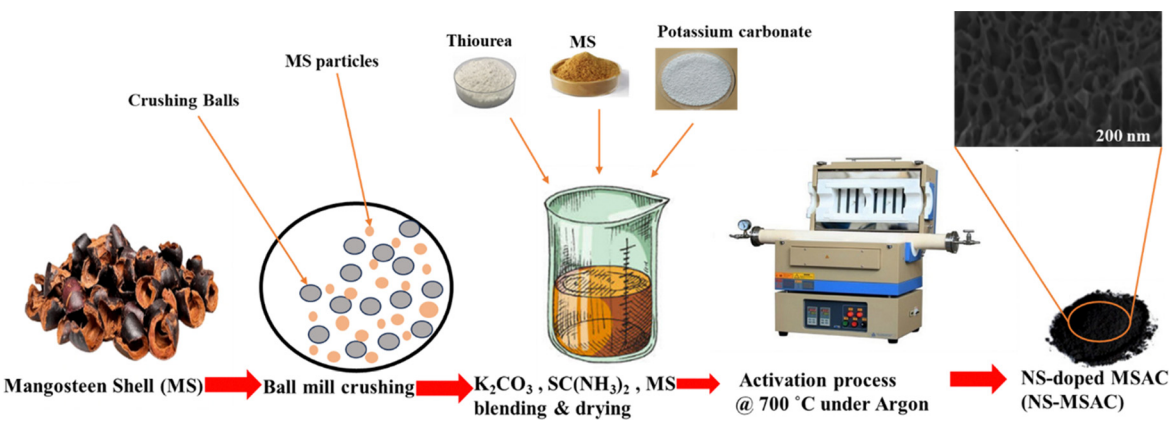

Scheme 1 Schematic diagram of the synthesis process for MSAC and NS-MSAC.[29,30]

hydrochloric acid for 5 hours, filtered, rinsed to neutral pH, and dried again at 60 °C for 12 hours.

The XRD patterns of MSAC and NSMSAC, shown in Fig. 1(a), exhibit similar patterns with two broad peaks at 2θ of 12.02° and 42.51°, corresponding to the (002) and (100) graphitic planes, typical of amorphous carbon. The increased peak widths in NSMSAC are attributed to heteroatom doping. Nitrogen and sulphur co-doping *via* thiourea introduces defects in the carbon structure, further reducing its crystallinity.[31] The Raman spectra that confirmed the degree of disorder in MSAC and NS-MSAC are illustrated in Fig. 1(b) with typical D (at cm^{-1}) and G (at cm^{-1}) bands of carbon.

The NOVA touch LX^2 Quanta Chrome Analyzer (NOVA Touch NT 2LX-1, 220 V, USA) was used to examine the specific surface area and pore size distribution. The adsorption–desorption isotherms of MSAC and NS-MSAC presented an isotherm type I featuring a hysteresis loop IV according to the IUPAC classification, suggesting the presence of micropore and mesopore structures in the synthesized materials (as displayed in Fig. 2(a) and (b)). The SEM pictures of NS-MSAC and MSAC (as insets in Fig. 2(a)) were examined with a Zeiss Ultra plus 55 field emission scanning electron microscope. As seen in the result, NS-MSAC and MSAC demonstrate outstanding interconnections and porous networks. 12 m $NaNO_3$ (m: mol kg^{-1}) was prepared by dissolving 20.39 g (0.24 mol) of $NaNO_3$ in 20 mL of deionized water. The solution was stirred for 6 hours to ensure the total dissolution of $NaNO_3$. The conductivity of 12 m $NaNO_3$ (167 mS cm^{-1}) was measured using a Jenco model 3020M conductivity meter (Jenco, USA) with an accuracy of ~0.5 F S at 20.2 °C. The viscosity of 12 m $NaNO_3$ (2.69 mPa s) was determined with an RV model NDJ-8S viscometer (W&J Instrument Co., PRC). The Biologic VMP300 potentiostat (made in the USA) equipped with the EC-Lab® software V11.50 was used in three-electrode and two electrode set-ups to evaluate the electrochemical performance of the electrode material using 12 m $NaNO_3$ as the electrolyte. To fabricate the working electrode, a mixture made of 80% active material (2.4 mg), 10% PVDF binder (0.3 mg) and 10% carbon black (0.3 mg) was employed. To make up for the conductivity that was lost when the nonconductive PVDF was added, carbon black was utilized. Two drops of *N*-methyl-2-pyrrolidone (NMP) were added to the mixture to create a slurry and homogenize it. The resulting slurry was pasted over the surface of a nickel foam current collector and left to dry at 60 °C overnight to guarantee that the binder evaporated entirely. The active material's mass loading ranged from 2.0 to 3.0 mg cm^{-2}. The three-electrode system consisted of a T-cell comprising the active electrode as the working electrode, an Ag disc as the reference electrode, and a glassy carbon disc as the counter electrode. The T-cell was used to assemble symmetric and asymmetric devices in a two-electrode arrangement with filter paper separating the electrodes that were co-doped with N and S and MS-AC. To examine the electrochemical performances of the working electrode, cyclic voltammetry (CV), galvanostatic charge–discharge (GCD), and electrochemical impedance spectroscopy (EIS) were utilized. The CV measurements were conducted at various scan rates spanning 5 to 100 mV s^{-1}, with potential windows of −1 to 0.0 V for the negative electrode and 0.0 to 1 V for the positive

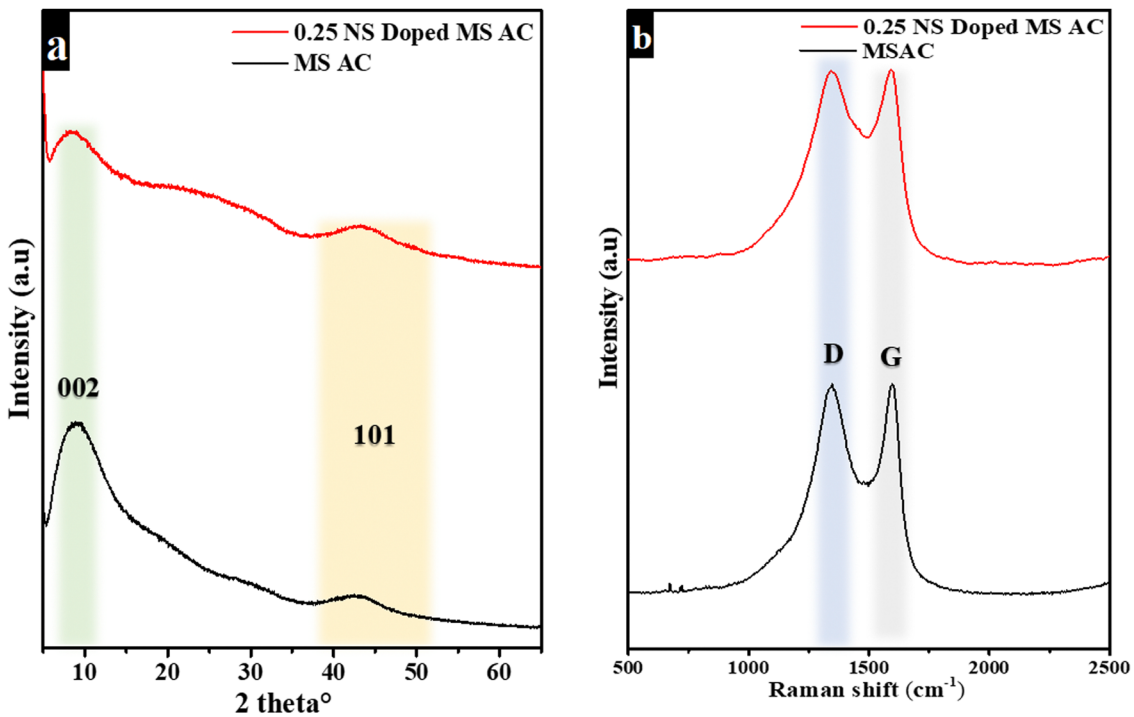

Fig. 1 (a) XRD patterns and (b) Raman spectra of MSAC and NS-MSAC.[29,30]

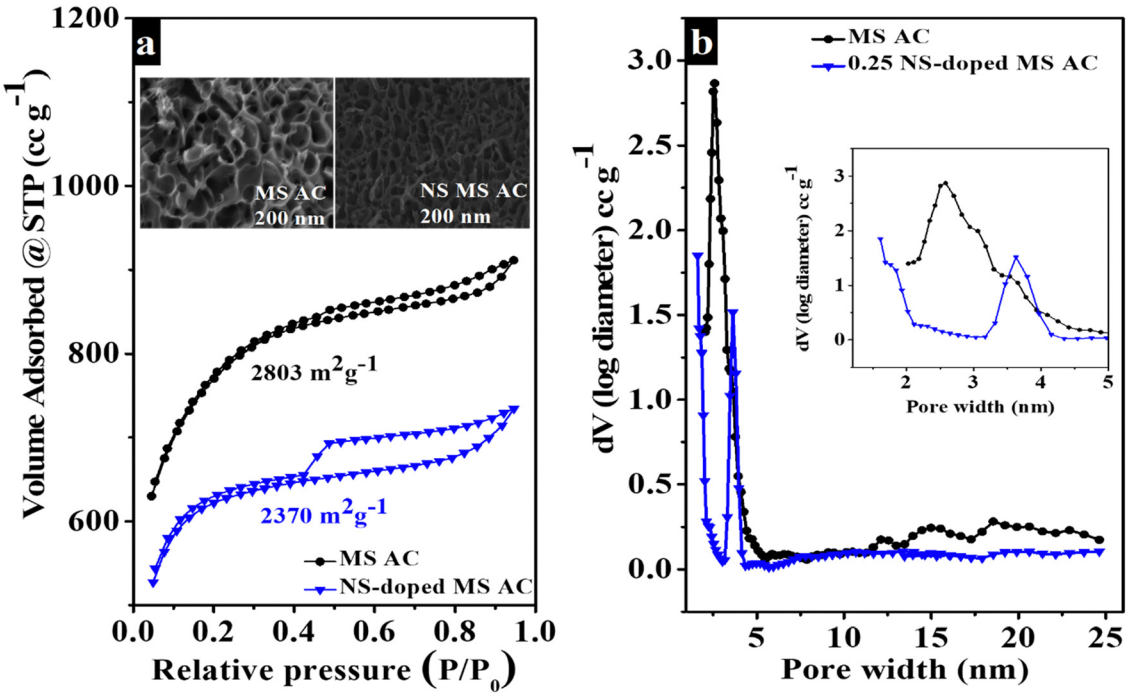

Fig. 2 MSAC & NS-MSAC (a) N_2 adsorption–desorption isotherms with SEM images given in the inset and the (b) pore size distribution.[29,30]

electrode. The galvanostatic charge–discharge measurements occurred at different specific currents ranging from 0.5 to 10 A g^{-1}. The EIS was measured at various frequencies from 10 MHz to 100 kHz. The EIS data measurements were evaluated using Nyquist plots. The specific capacitance (C_{sp}) in a three-electrode set-up for the EDLC material is calculated using the slope of GCD curves using the following equation:[32]

$$C_{sp}(\text{three}) = \frac{I\Delta t}{m\Delta V}\ (\text{F g}^{-1}) \quad (2)$$

where I, Δt, m, and ΔV indicate the applied current, the discharge time, the electrode mass, and the potential window, respectively.

The single electrode capacitance C_S, the energy density E_d, the power density P_d and the coulombic efficiency η of the two electrode system are evaluated from the GCD profile according to the following formulas:[33]

$$C_s(\text{two}) = \frac{4I\Delta t}{m\Delta V}\ (\text{F g}^{-1}) \quad (3)$$

$$E_d = \frac{C_{sp}(\text{two}) \times V^2}{8 \times 3.6}\ (\text{W h kg}^{-1}) \quad (4)$$

$$P_d = \frac{3600 \times E_d}{\Delta t}\ (\text{W kg}^{-1}) \quad (5)$$

$$\eta = \frac{t_d}{t_c} \quad (6)$$

where I, Δt, m, ΔV, t_d and t_c represent respectively the applied current density, discharging time, total mass of both electrodes, voltage, discharging time and charging time.

To balance the charges in a device, the mass balance equation is necessary due to the differences in the working potential and charge–discharge time between the positive and negative electrodes. Thus, the following equation was used to balance the charges:[34]

$$\frac{m_+}{m_-} = \frac{C_{s-}\Delta V_-}{C_{s+}\Delta V_+} \quad (7)$$

3. Electrochemical discussion

3.1. Half-cell (three-electrode) analysis results

The electrochemical performances of MSAC and NS-MSAC materials in the 12.0 m $NaNO_3$ WIS electrolyte were assessed in a three-electrode set-up using cyclic voltammetry (CV), galvanostatic charge–discharge (GCD) and electrochemical impedance spectroscopy (EIS). The CV curves at 20 mV s^{-1} and the GCD curves at 0.5 A g^{-1}, accompanied by their relative performance capabilities in the negative (−1–0 V *vs.* Ag) and positive (0–1 V *vs.* Ag) potential ranges, and EIS are displayed in Fig. 3. Fig. 3(a) shows that all CV profiles of the tested electrodes at a scan rate of 20 mV s^{-1} exhibit rectangular shapes, indicating electric double-layer capacitor (EDLC) performance. However, the NS-MSAC (purple curve in the negative and red curve in the positive) displays a quasi-rectangular shape with additional broad peaks especially in the positive, suggesting supplementary redox reactions occurring on the electrode surface due to N and S dopants. The CV curves reveal that the current response of the NS-MSAC was larger than that of MSAC at 20 mV s^{-1}, showing that the NS-MSAC had a higher specific capacitance. This is owing to the electrochemical oxidation–reduction process induced by the presence of the nitrogen and

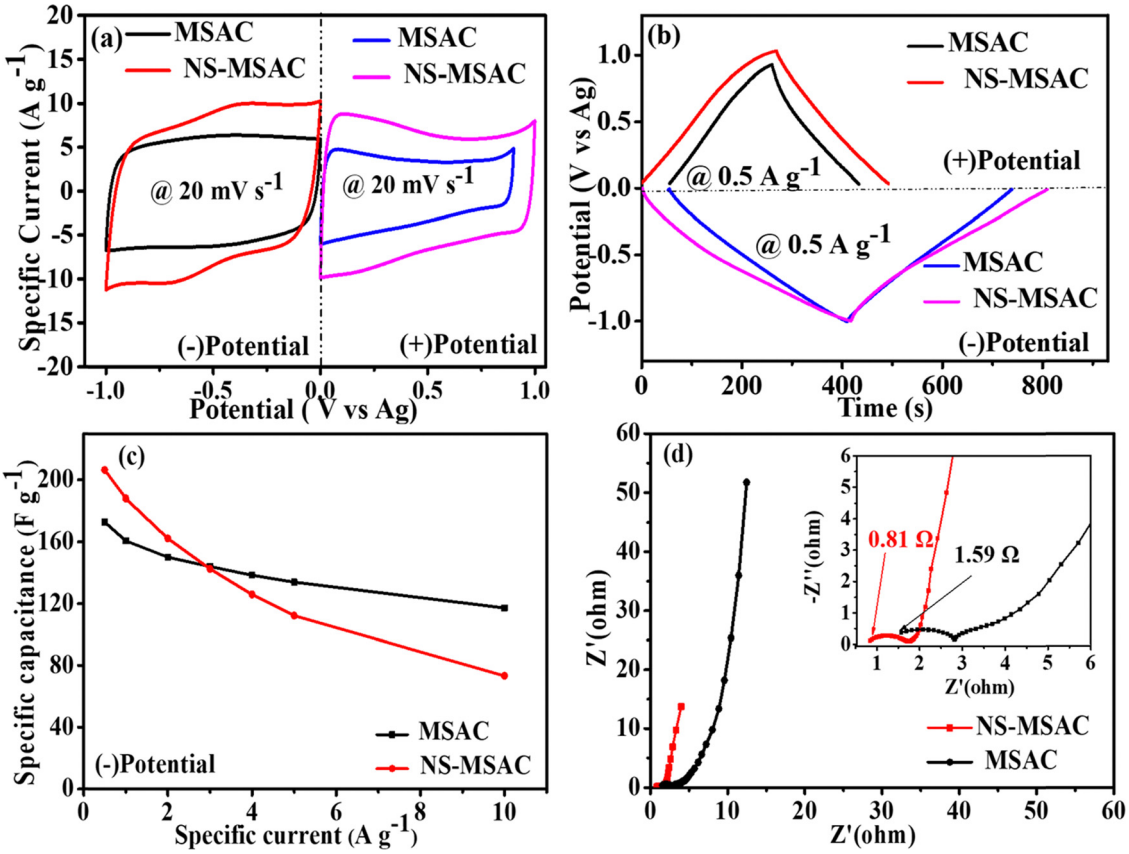

Fig. 3 (a) CV curves at 20 mV s^{-1}, (b) GCD curves at 0.5 A g^{-1}, (c) specific capacitance *vs.* specific current, (d) Nyquist plot for MSAC and NS-MSAC samples.

sulphur functional groups. Additionally, compared to the undoped activated carbon, NS-MSAC exhibits a broader positive potential window (1.0 V *vs.* Ag). This can be explained by the limiting activity of water in aqueous solutions through the application of the 12.0 m $NaNO_3$ water-in-salt electrolyte. The increased ESW of 12 m $NaNO_3$ can be attributed to its distinct water structure compared to dilute aqueous electrolytes. In aqueous electrolytes, dissolved ions influence the H-bonding structure of water molecules in the initial hydration shell of each ion (cations and ions from the salt).[35] In 12 m $NaNO_3$, the number of free water molecules decreases. Many water molecules are confined in a Na^+ solvation layer, which disrupts hydrogen bonding between water molecules, resulting in stronger O–H bonds inside individual water molecules, inhibiting hydrogen evolution. Oxygen and hydrogen evolution appeared to be suppressed as the salt concentration increased, which is probably due to the decreased water activity when sodium ions combine with water molecules at high concentrations.[36,37] Nevertheless, because of the low H^+ concentration, heteroatom-doped carbon displays a large over-potential in a neutral electrolyte that demonstrates higher potential for hydrogen and oxygen evolution, leading to enhancement in the potential window.[38] The GCD curves, shown in Fig. 3(b), obtained at a specific current of 0.5 A g^{-1} show triangular linear charge–discharge profiles for both samples in the negative and positive potential windows, confirming the EDLC and pseudo behaviours illustrated in Fig. 3(a). The NS-MSAC electrode has a longer discharge time compared to the undoped MSAC, which correlates with the present CV profiles and confirms the sample's enhanced charge storage capacity. For MSAC and NS-MSAC, the maximum specific capacitances determined from the discharge curves using eqn (2) were 172.93 F g^{-1} and 206 F g^{-1} at a current density of 0.5 A g^{-1}, respectively. The NS-MSAC sample has the highest specific capacitance, which is in accordance with its largest current response from the CV curves. Nitrogen functional groups on N heteroatoms can provide sustained pseudo capacitance through amine group redox reactions. These amine groups have good electron–donor properties and better charge mobility and influence the electron transport through the carbon framework.[39] Due to their electron-rich nature, S heteroatoms can significantly increase the interlayer distances of NS-MSAC, providing more polarized surfaces and reversible pseudo sites, and thus produce extra pseudo capacitance. Furthermore, the inclusion of S atoms facilitates N functional groups' redox reactions, which improves electrochemical performance.

The increased wettability of the electrode material is another benefit of sulphur doping.[40] The insertion of nitrogen and sulphur into the carbon framework results in better wettability, higher conductivity and more pseudo capacitance which contribute to the superior specific capacitance performance of the NS-MSAC material. In other words, N and S co-doping raises the

ion kinetics within the micropores and enhances interactions between doped sites and electrolyte ions, which increases surface/interface accessibility and significantly raises the electrical double-layer capacitance.[41,42] The correlation between the specific capacitance and specific current of the active materials was assessed using GCD measurements, conducted over a range of 0.5 to 10 A g^{-1} in the negative potential region, with the results illustrated in Fig. 3(c). NS-MSAC had a high specific capacitance of 117 F g^{-1} at 10 A g^{-1}, but NS-MSAC only had 72 F g^{-1} at 10 A g^{-1}. The explanation could be that with higher specific currents, there is not enough time for ions to migrate, aggregate, and diffuse towards the surface and inner pores of the active materials, resulting in a drop of capacitance response during the quick charge and discharge processes.[43,44] To acquire a thorough comprehension of the charge transfer and ion diffusion in electrodes, Nyquist plots are employed. Fig. 3(d) indicates the MSAC and NS-MSAC samples' Nyquist plots in the 12.0 m $NaNO_3$ electrolyte. The equivalent series resistance (ESR) is given by the intercept with the x axis at high frequency ranges. The electrode surface resistance (ESR) is a crucial characteristic for supercapacitor materials as it reveals the resistance between the electrode material and the current collector as well as the resistance between the working electrode and ions from the electrolyte. Because of the higher potential drop, supercapacitor performance may be adversely affected by high ESR values. NS-MSAC has the lowest equivalent series resistance (ESR = 0.81 Ω) compared to MSAC (ESR = 1.59 Ω). The reduced ESR in NS-MSAC indicates improved electrical conductivity and less resistance at the interface of the electrode and electrolyte, and the electrode–current collector interfaces. Furthermore, the high-frequency semicircle represents the charge-transfer resistance (R_{ct}) generated on the surface of the active material. The NS-MSAC has a lower R_{ct} (0.95 Ω) value compared to MSAC (1.50 Ω) based on the semicircle estimation. The NS-MSAC sample has shorter diffusion lengths, showing faster ion diffusion at the electrode/electrolyte interface compared to the pristine activated carbon which provides beneficial properties for the capacitive material. The high conductivity and wettability of the electrode material's surface reduce the diffusion resistance between the electrode and the electrolyte ions. Electrolyte ions can easily access porous materials as illustrated by the low R_{ct} of NS-MSAC.[45,46] Furthermore, the NS-MSAC Nyquist plot curve demonstrates superior EDLC capacitive performance, with a nearly parallel straight line to the imaginary axis, whereas MSAC has an almost vertical line. The NS-MSAC's low resistance is due to the integration of heteroatom-doped carbon, which induces a large contact surface and ion transport.

Dunn's approach was used to investigate the contribution of all EDLC and pseudocapacitive samples in a 12.0 m $NaNO_3$ water-in-salt electrolyte to acquire an exhaustive understanding of the capacitive behaviour of the NS-MSAC and MSAC materials as depicted in Fig. 4 and 5. Activated carbon contributed to the majority of the EDLC behaviour, and heteroatom doping such as N and S contributed to the greater surface functionality, as evidenced by the pseudocapacitive features observed. By applying Dunn's method and analyzing the cyclic voltammetry data at different scan rates, the capacitive contributions were calculated using eqn (11),[47]

$$i = a\nu^b \quad (8)$$

where i the measured current density has a power law relationship with the scan rate ν. Both a and b are changeable parameters, in which the b-values can be determined by the slope of the $\log i$ *vs.* $\log \nu$ plot. Surface capacitance-dominated systems have b values around 1.0, whereas diffusion -controlled processes typically have their b values near to 0.5. The MSAC and the NS-MSAC have a and b values of 0.990 and 0.945, respectively (as depicted in Fig. 4(a) and (b), indicating an excellent capacitance-dominated system.

Fig. 4 and 5 present the surface-controlled (cyan colour) and the diffusion-controlled (magenta colour) contributions and their contributions at different scan rates. MSAC has a larger EDLC contribution in capacitance for surface-controlled (95.2%) than NS-MSAC (74.7%) at 5 mV s^{-1} (as shown in Fig. 4(c), (d) and 5(a), (d). Increasing the scan rate gradually enhances the surface-controlled and decreases the diffusion-controlled effect caused by redox processes. The MSAC has a diffusion-controlled rate of less than 2% at 50 mV s^{-1}. The EDLC accounts for almost all the capacitances. At high scan rates, the ions inside the electrode don't have enough time to diffuse toward the surface and the inner pores of the active materials, so it's evident that the diffusion-controlled is decreasing. As the results are compared to a low scan rate, NS-MSAC presents less diffusion-controlled at high scan rates. NS-MSAC has a surface-controlled rate of 90.3% at 50 mV s^{-1} as displayed in Fig. 4(d) and 5(f). The NS-MSAC sample exhibits a much higher percentage of pseudo capacitance in 12.0 m $NaNO_3$ WIS as compared to the MSAC sample. This is due to the N and S dopants providing additional pseudo-capacitive behaviour. Functional groups comprising nitrogen (pyridinic-N and pyrrolic-N) and sulfur (sulfonyl –C–SO_2–C– and thiophene –C–S–C–) employed during the doping process improve the pseudo-capacitive performance of activated carbons used in supercapacitors. The suggested pseudo-capacitance may have happened *via* the reversible faradaic reactions given below:[48]

$$C{=}N + H^+ + e^- \leftrightarrow C{-}NH \quad (9)$$

$$C{-}SO_2{-}C + 2e^- \leftrightarrow C{-}SO{-}C \quad (10)$$

$$C{-}SO{-}C + e^- \leftrightarrow C{-}SOH{-}C \quad (11)$$

Furthermore, surface-controlled contributions outperformed the diffusion-controlled redox contributions when charge storage contributions were determined at low and high scan rates, confirming that EDLC storage mechanisms are dominant in both MSAC and NS-MSA.

3.2. Full cell (two-electrode system measurement)

To assess the practical viability of carbon electrodes in highly concentrated aqueous electrolytes, we assembled three supercapacitor devices – symmetric NS-MSAC//NS-MSAC and

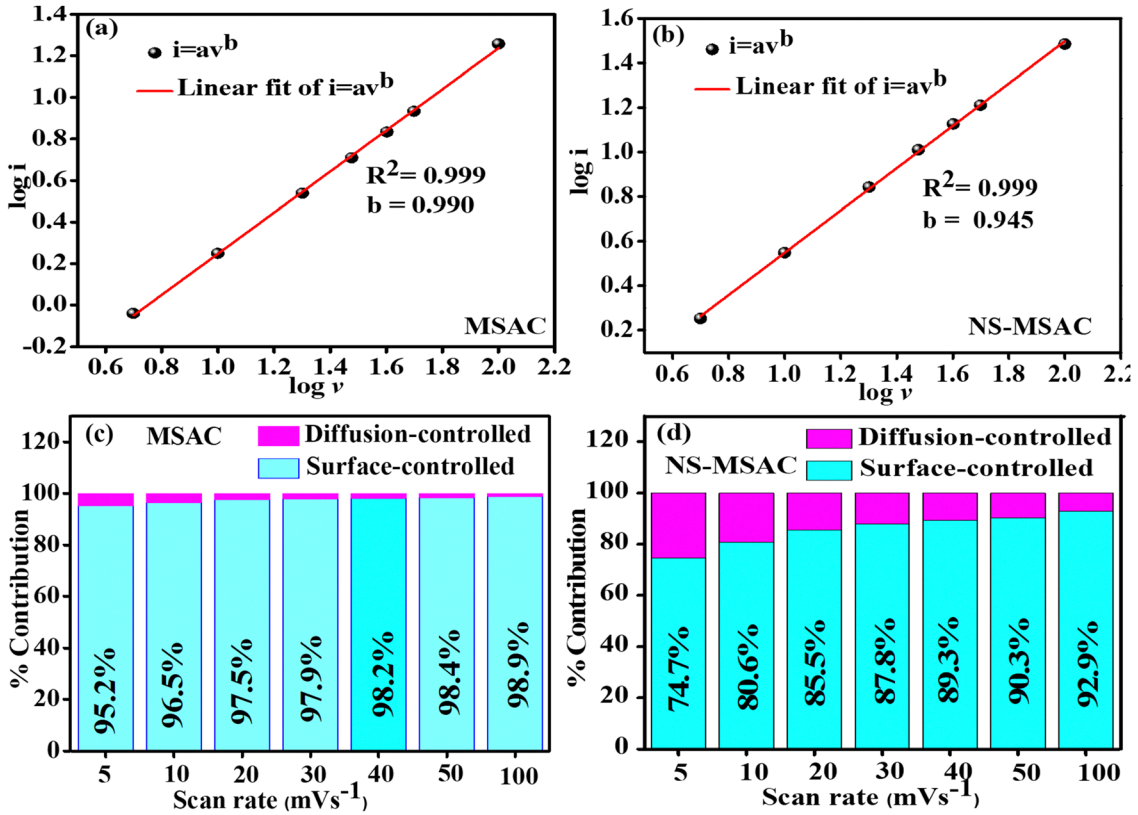

Fig. 4 Plot of the (a) log peak current density against log scan rate for MSAC, (b) log peak current against log scan rate for NS-MSAC, (c) surface-controlled contribution and diffusion-contribution of MSAC and the (d) surface-controlled contribution and diffusion-controlled contribution of NS-MSAC.

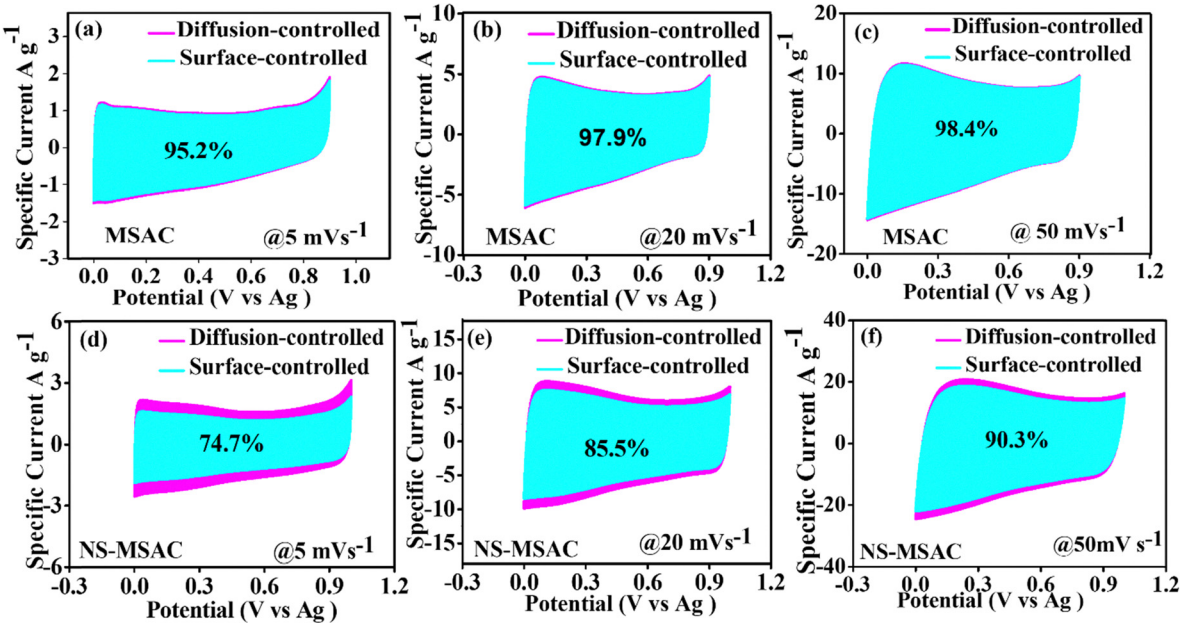

Fig. 5 CVs showing surface-controlled and diffusion-controlled contributions (a)–(c) for MSAC and (d)–(f) for NS-MSAC at 5 mV s^{-1}, 20 mV s^{-1} and 50 mV s^{-1}, respectively.

MSAC//MSAC, and asymmetric NS-MSAC//MSAC using 12.0 m $NaNO_3$ as the electrolyte. The masses of the electrode materials were balanced to attain equal charge contribution by using eqn (7). This was done according to the variations in the

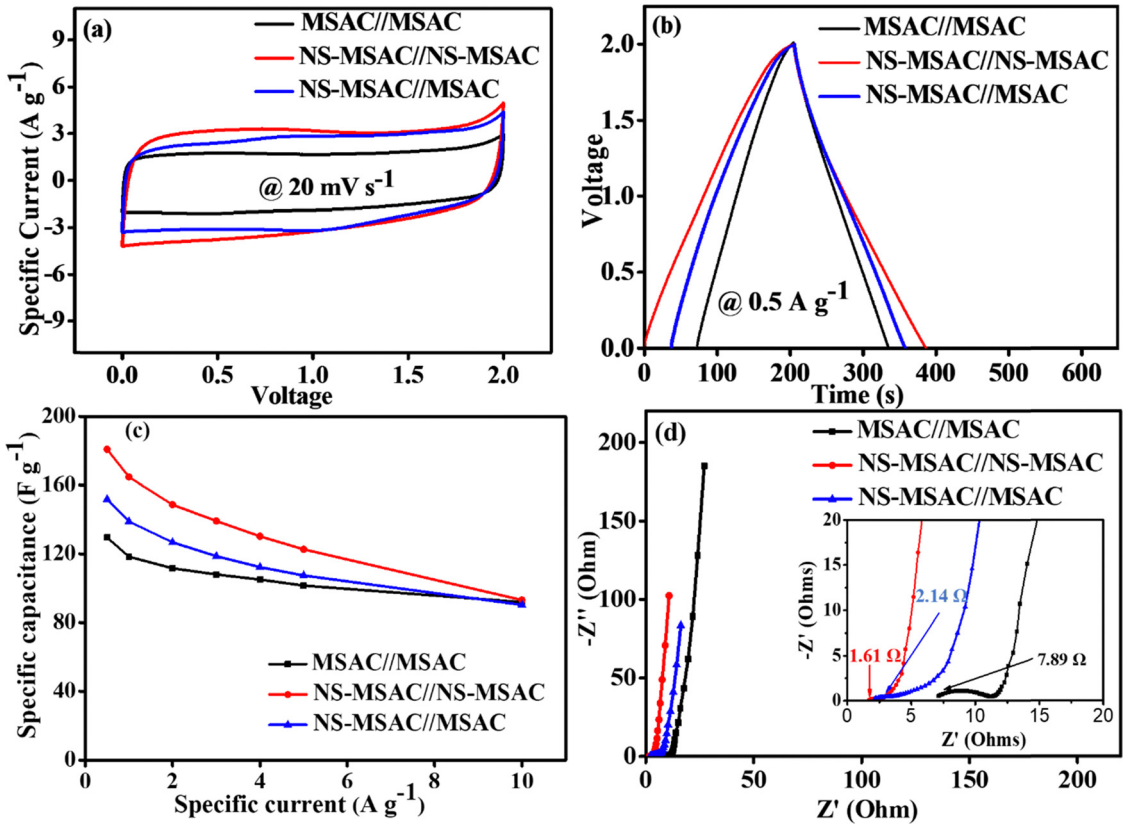

Fig. 6 (a) CV curves at 20 mV s^{-1}; (b) GCD curves at 0.5 A g^{-1}; (c) specific capacitance *vs.* specific current and the (d) Nyquist plot for all devices are indicated in the figure.

potential windows and charge/discharge rates in the three electrode measurement for NS-MSAC and MSAC. The operative areal mass of the assembled devices, including both the positive and negative electrodes (NS-MSAC or MSAC), was approximately 4.3 mg cm^{-2} per device. Fig. 6(a) displays the CV curves for devices using the 12.0 m $NaNO_3$ electrolyte at a scan rate of 20 mV s^{-1} in two-electrode measurements. All devices exhibit an electrochemical cell voltage of 2.0 V, as determined from the positive and negative potential limits. The water-in-salt electrolyte causes the high cell voltage by delaying the kinetics of hydrogen and oxygen synthesis on the anode and cathode, respectively. This is advantageous for the high specific energy of supercapacitors. The NS-MSAC//NS-MSAC has the highest current response, which suggests that the device's ionic conductivity has improved. The GCD curves for all the assembled devices were obtained as illustrated in Fig. 6(b). The figure shows the EDLCs' characteristic behaviour, exhibiting symmetrical charge–discharge paths with all the devices, indicating ideal capacitive performance. A prolonged discharge time is exhibited by the NS-MSAC//NS-MSAC. The specific capacitance derived from the GCD curves at 0.5 A g^{-1} using eqn (3) reveals that NS-MSAC//NS-MSAC maintains the highest specific capacitance (C_{sp} = 180 F g^{-1}) compared to NS-MSAC//MSAC (C_{sp} = 148 F g^{-1}) and MSAC//MSAC (C_{sp} = 128 F g^{-1}). The rate capabilities of all the devices illustrating a comparison of their specific capacitances at various specific currents are illustrated in Fig. 6(c). All devices show reduced capacitances with increasing current densities. This can be explained by the fact that the controlled diffusion effect gradually decreases at a high current density, as shown by the Dunn method, due to the presence of doping heteroatoms. Additionally, the electrolyte ions do not have enough time to reach the pores in the carbon material indicating that only a portion of the electrolyte ions may enter the electrode pores at a high current density. To gain a deeper comprehension of the supercapacitor's performance, EIS was used to analyse the electrochemical behaviour of the supercapacitors. Fig. 6(d) depicts the Nyquist plots for NS-MSAC//NS-MSAC, NS-MSAC//MSAC, and MSAC//MSAC devices in 12 m $NaNO_3$ electrolytes. All the devices have a Nyquist plot consisting of a semi-circle at high frequencies and a linear slope at low frequencies. A semicircle with a little curvature, a short diffusion path and slope at the *y*-axis, and an equivalent series resistance (ESR) on the *x*-axis (*Z*-axis) that approaches zero are the characteristics of EDLC materials.[49] The charge transfer resistance (R_{ct}) which is the point of intersection on the right-hand side of the semicircle provides further details related to the reactions that take place at the interface between the electrode and electrolyte. R_{ct} values of 0.17, 1.64 and 3.44 Ω were obtained for the NS-MSAC//NS-MSAC, NS-MSAC//MSAC, and MSAC//MSAC devices, respectively. The equivalent series resistance values, determined by the intersection of the diffusion path with the *x*-axis, were 1.61 Ω for NS-MSAC//NS-MSAC,

2.14 Ω for NS-MSAC//MSAC, and 7.89 Ω for MSAC//MSAC, respectively. These features demonstrate that NS-MSAC//NS-MSAC has the highest ion mobility rate out of the three devices tested. These results confirm that N and S doping heteroatoms significantly improve the mobility of ions in highly concentrated WIS electrolytes.

The lifespan of the electrode material is a critical factor in the performance of a supercapacitor. Fig. 7(a) shows the cycling performance of NS-MSAC//NS-MSAC, NS-MSAC//MSAC, and MSAC//MSAC at 5 A g^{-1}. Within 8000 cycles, the NS-MSAC/NS-MSAC device exhibits exceptional cyclability. It retains 85% of its initial capacitance, whereas NS-MSAC//MSAC and MSAC//MSAC retain 77% and 70% of their original capacitance, respectively. Fig. 7(b) plots the coulombic efficiency *vs.* cycle number for the devices at 5 A g^{-1}. The stability was verified over 8000 charge–discharge cycles. The device's coulombic efficiency (C_E) was estimated using the following equation:[33]

$$\eta = \frac{t_d}{t_c} \times 100 \quad (12)$$

where t_c and t_d denote the charging and discharging times at the same specific current, respectively. NS-MSAC//NS-MSAC demonstrated a coulombic efficiency of 99.6%, while NS-MSAC//NS-MSAC and MSAC//MSAC had 99.46% and 99.22%, respectively. Fig. 7(c) depicts a Bode plot of the various devices built in a 12 m $NaNO_3$ water-in-salt electrolyte. The NS-MSAC//NS-MSAC cell exhibits superior supercapacitive behaviour, with a phase angle of −84° at lower frequencies, which is closer to the ideal supercapacitive phase angle of −90° making it ideal for capacitive applications. NS-MSAC//MSAC and MSAC//MSAC have a phase angle of −80, also indicating good capacitive properties.

Fig. 8(a) displays the CV curves of the device NS-MSAC//NS-MSAC measured at scan rates ranging from 5 to 100 mV s^{-1}. The CV curves show a quasi-rectangular form, indicating EDLC behaviour. The capacitive response remained stable with an increase in the scan rate while maintaining a rectangular shape. The symmetric device NS-MSAC//NS-MSAC exhibits excellent ion diffusion and rapid ion transport between the active materials and current collector. This reveals that the device's material has a low contact resistance, resulting in increased electrical conductivity due to the presence of doping heteroatoms. The device operated at a voltage of 2.0 V, confirming the distinctive behaviour of the 12 m $NaNO_3$ water–in-salt electrolyte that limits the water activity with lower free water in 12 m $NaNO_3$ compared to the salt in water electrolytes. WIS can lead to an increase in the potential of hydrogen and oxygen evolution. Fig. 8(b) illustrates the GCD curves of the symmetric device NS-MSAC//NS-MSAC for various current densities ranging from 0.5 to 10 A g^{-1}. The triangular pattern depicts a double layer capacitor. It could operate in the same voltage window of 2.0 V with a minimal IR drop. The NS-MSAC//NS-MSAC capacitance *vs.* specific current was determined from GCD curves using eqn (2), as shown in Fig. 8(c). The symmetric device achieved a maximum specific capacitance of 180 F g^{-1} at 0.5 A g^{-1} and maintained 92 F g^{-1} even at a high specific current of 10 A g^{-1}. After 8000 cycles, NS-MSAC//NS-MSAC demonstrated a superior coulombic efficiency of 99.6%, near to 100% at 5 A g^{-1}. The EIS

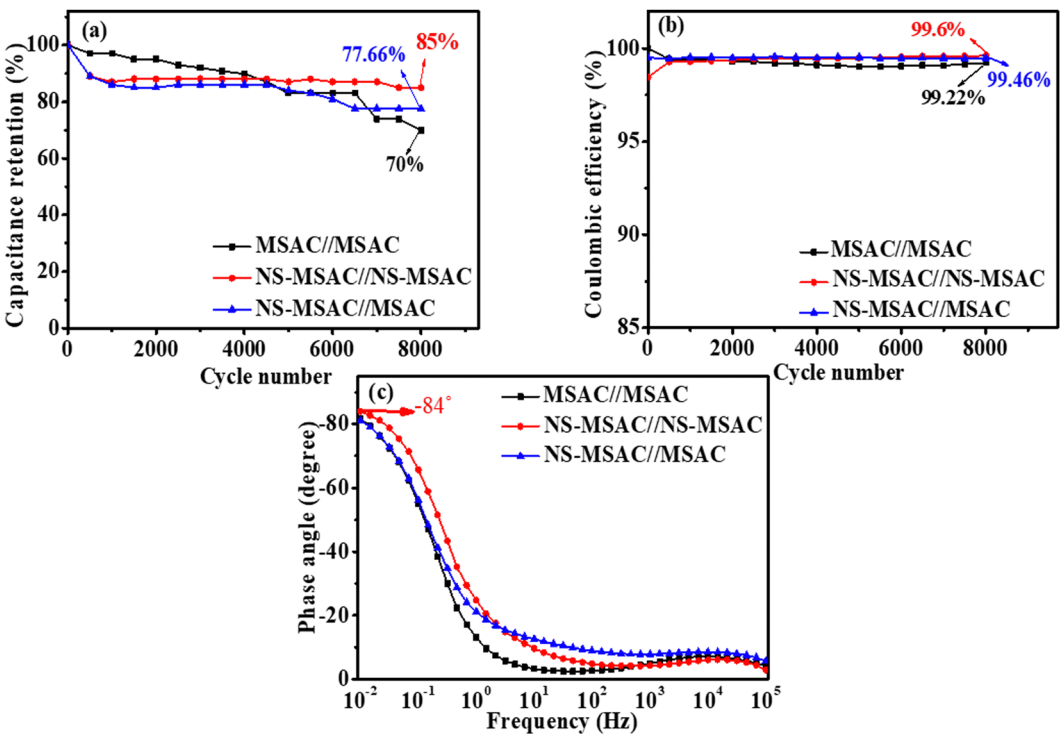

Fig. 7 (a) Capacitance retention against cycle number, (b) coulombic efficiency *vs.* cycle number and (c) Bode plots for all devices.

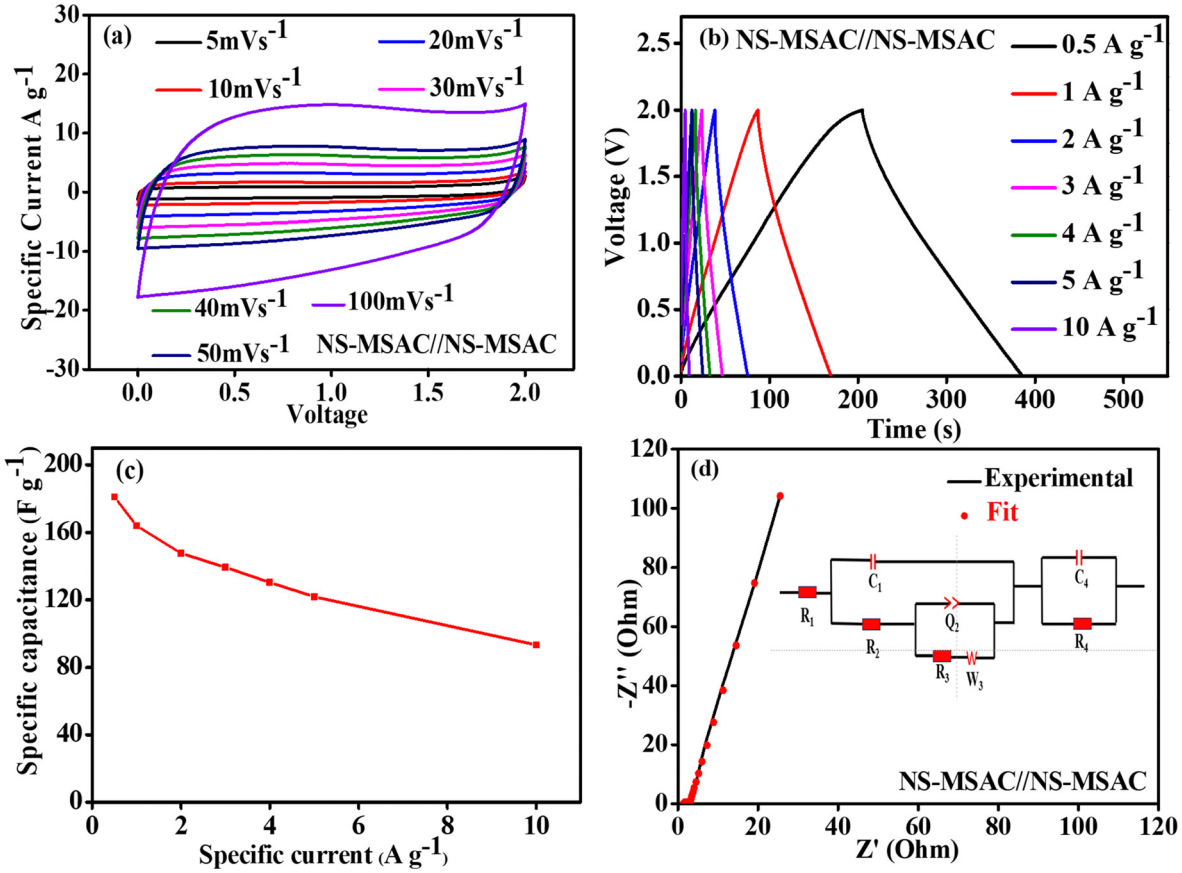

Fig. 8 (a) CV curves at different scan rates, (b) GCD curves at different specific currents, (c) specific capacitance *versus* specific current- and the (d) Nyquist plot (with the inset showing the equivalent circuit diagram used for the fitting of data).

plot for the NS-MSAC//NS-MSAC cell was fitted, as shown in Fig. 8(d), using the Z-fit from the software @EC lab V11.50, with the corresponding electrical circuit displayed as an inset to the figure. The equivalent electrical circuit shows that R_1 represents the equivalent series resistance (ESR), while C_1 and C_4 represent the double layer capacitance interface and the pseudo capacitance resulting from ion charge transfer. The constant phase element Q_2 and the Warburg diffusion element W are connected in series with R_4, which symbolizes the R_{ct}. Because the divergence from the y axis is not considerable, the leakage resistance (R_L) represented by R_3 in the circuit is responsible for the Nyquist plot's deviance from the imaginary axis. In this situation, R_L is tiny. The ESR and R_{ct} values obtained from the fitting EIS were 1.412 and 0.878 Ω, which are comparable to the experimental values of 1.61 and 0.17 Ω suggesting a good match between the Nyquist plot and the Z fit EIS.

The capacitor retained 85% of its specific capacitance even after 8000 cycles (Fig. 9(a)). The reported 85% capacitance retention can be attributed to the ease of passage of the electrolyte ions owing to the improved electrical conductivity, providing for several charge/discharge cycles. A gradual reduction is noticeable at about 500 cycles due to the partial collapse of some pores in the active material, resulting in a drop for the specific capacitance. Fig. 9(b) shows the frequency-dependent real ($C'(\omega)$) and imaginary ($C''(\omega)$) capacitances obtained from eqn (14) and (15), where $Z(\omega)$ is the impedance $Z(\omega)$ with $\omega = 2\pi f$[50]

$$Z(\omega)\frac{1}{j(\omega) \times C(\omega)} \quad (13)$$

$$C'(\omega)\frac{Z''(\omega)}{\omega|Z(\omega)|^2} \quad (14)$$

$$C''(\omega)\frac{Z'(\omega)}{\omega|Z(\omega)|^2} \quad (15)$$

$$Z(\omega) = Z'(\omega)^2 + Z''(\omega)^2 \quad (16)$$

The graph reveals a real accessible capacitance ($C'(\omega)$) of 0.12 F and an imaginary capacitance $C''(\omega)$ resulting in a relaxation time ($\tau = 1/2\pi f$, where f is the peak frequency) of 0.23 s at 0.636 Hz, signifying that the device can quickly and effectively charge and discharge in a short time Fig. 9(c) illustrates the relationship between the phase angle and frequency. The phase angle is approximately 84 (the ideal value is 90), indicating that the functioning of the cell is nearly identical to that of an ideal capacitor. Ragone's plot [Fig. 9(d)] depicts the correlation between the specific energy and specific power of the symmetrical NS-MSAC//NS-MSAC supercapacitor cell at various

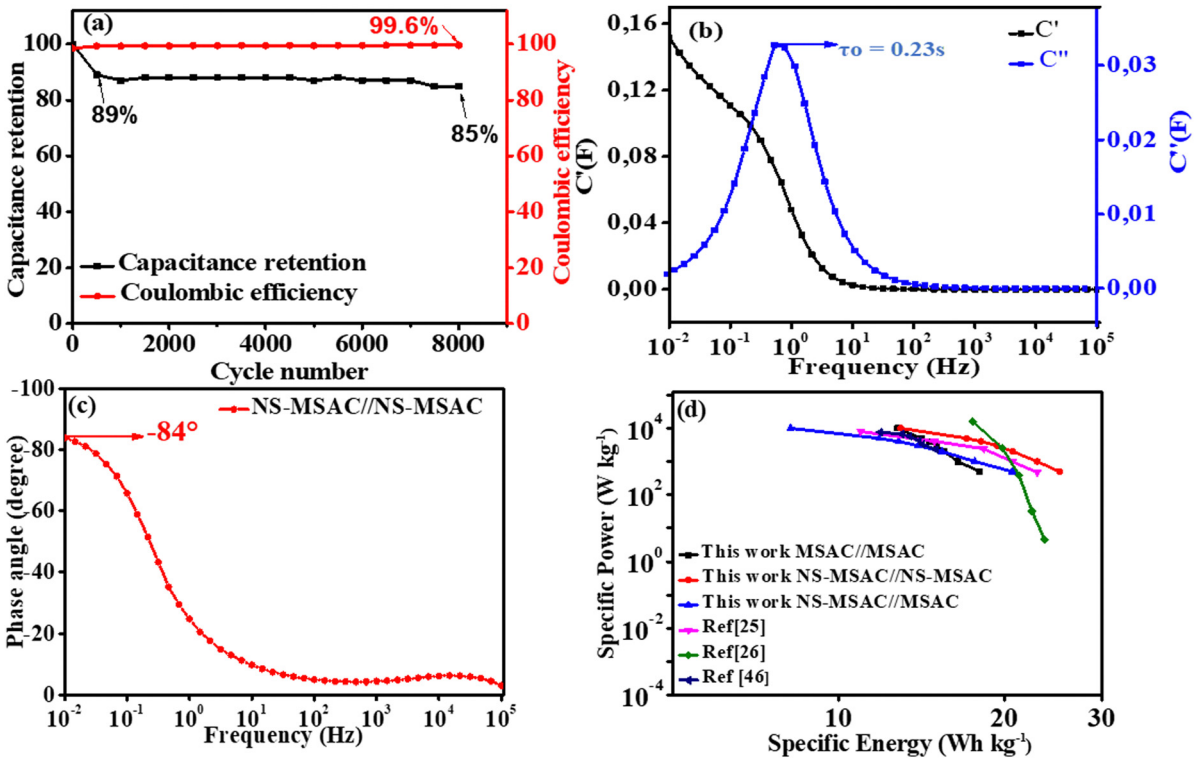

Fig. 9 (a) Capacitance retention and coulombic efficiency against cycle number, (b) real and imaginary capacitance against frequency, (c) Bode plot and (d) Ragone plot.

Table 1 Water-in-salt electrolyte symmetric devices' performance comparison

Material	Electrolyte	C_{single} (F g^{-1})	Cell voltage (V)	ES (W h kg^{-1})	P_s (W kg^{-1})	Ref.
AC//AC	5 m LiTFSI	143	2.5	24	480	52
N/SCSAC//N/SCSAC	25 m KAC	—	2.94	48.86	—	53
AC//AC	17 m $NaClO_4$	—	2.3	23.7	—	54
AC//AC	31.3 m	—	2.4	30	228	55
AC//AC	8 m NaTFSI	170	1.8	14.4		56
AC//AC	12 m $NaNO_3$	—	2.1	20.5	—	57
NSMSAC//NSMSAC	12 $NaNO_3$	206	2.0	25	512	This work

current densities. The NS-MSAC//NS-MSAC symmetrical cell delivered an energy density of 25 W h kg^{-1} with a power density of 512 W kg^{-1} at a specific current of 0.5 A g^{-1}, which is higher than those obtained with the two additional devices, which displayed maximum energy specific values of 21.1 W h kg^{-1} for the asymmetrical device of NS-MSAC//MSAC and 18.01 W h kg^{-1} for MSAC//MSAC at 0.5 A g^{-1}. The NS-MSAC//NS-MSAC device using 12 m $NaNO_3$ exceeds or matches the similar previously reported devices. The results were largely attributed to the beneficial properties of 12 m $NaNO_3$ WIS, which include the smaller ion size of NO_3^- (179 pm), as well as the better conductivity and adequate viscosity of $NaNO_3$, which increase ion accessibility at the electrolyte/electrode interphase.[51] In addition, the application of 12 m $NaNO_3$ substantially increases the cell voltage while decreasing water activity. In addition, co-doping N and S not only enhances conductivity and wettability, but also adds capacitance through redox processes, which enhanced the total capacitance (Table 1).

4. Conclusion

In conclusion, we have demonstrated the complementary effects of applying N and S co-doped activated carbon when combined with a high concentration aqueous salt (12 m $NaNO_3$) on electrochemical energy storage performance. With nitrogen and sulphur functionalities, the carbon material could exhibit a capacitance of 206 F g^{-1}, demonstrating exceptional cycle stability (85% after 8000 cycles) making it a great electrode material for energy storage. As result the NS-MSAC//NS-MSAC supercapacitor showed outstanding performances. The devices

have a specific capacitance of 180 F g^{-1} with specific energy and specific power values of 25 W h kg^{-1} and 512 W kg^{-1} at 0.5 A g^{-1}, respectively. The specific energy and power at 10 A g^{-1} were determined to be 12.94 W h kg^{-1} and 10 kW kg^{-1}, respectively. The high coulombic efficiency of 99.6% and capacitance retention of 85% after 8000 cycles demonstrate exceptional stability.

Data availability

Data can be available upon request from the authors.

Conflicts of interest

There are no conflicts to declare.

Acknowledgements

The authors acknowledge the University of Pretoria, South Africa, for providing research facilities. S. Thior also expresses gratitude for the financial support received through the UP Doctoral Research Bursary.

References

1 P. Simon and Y. Gogotsi, Materials for electrochemical capacitors, *Nat. Mater.*, 2008, **7**, 845–854, DOI: **10.1038/nmat2297i**.
2 L. Luo, Y. Lan, Q. Zhang, J. Deng, L. Luo, Q. Zeng, H. Gao and W. Zhao, A review on biomass-derived activated carbon as electrode materials for energy storage supercapacitors, *J. Energy Storage*, 2022, **55**, 105839, DOI: **10.1016/j.est.2022.105839**.
3 A. Bello, O. O. Fashedemi, J. N. Lekitima, M. Fabiane, D. Dodoo-Arhin, K. I. Ozoemena, Y. Gogotsi, A. T. Charlie Johnson and N. Manyala, High-performance symmetric electrochemical capacitor based on graphene foam and nanostructured manganese oxide, *AIP Adv.*, 2013, **3**, 8, DOI: **10.1063/1.4819270**.
4 H. Liao, L. Zhong, H. Zeng, Y. Xiao, B. Cheng and S. Lei, A dual-acetate synchronous catalysis-activation strategy towards regulable porous graphitic carbon for high-energy supercapacitor with acetate water-in-salt electrolyte, *Carbon*, 2023, **213**, 118305, DOI: **10.1016/j.carbon.2023.118305**.
5 X. L. Zhang, C. N. Feng, H. P. Li and X. C. Zheng, N, O self-codoped hierarchical porous carbon from chitosan for supercapacitor electrode active materials, *Cellulose*, 2021, **28**, 437–451, DOI: **10.1007/s10570-020-03536-5**.
6 O. Fasakin, J. K. Dangbegnon, D. Y. Momodu, M. J. Madito, K. O. Oyedotun, M. A. Eleruja and N. Manyala, Synthesis and characterization of porous carbon derived from activated banana peels with hierarchical porosity for improved electrochemical performance, *Electrochim. Acta*, 2018, **262**, 187–196, DOI: **10.1016/j.electacta.2018.01.028**.
7 N. F. Sylla, N. M. Ndiaye, B. D. Ngom, D. Momodu, M. J. Madito, B. K. Mutuma and N. Manyala, Effect of porosity enhancing agents on the electrochemical performance of high-energy ultracapacitor electrodes derived from peanut shell waste, *Sci. Rep.*, 2019, **9**, 13673, DOI: **10.1038/s41598-019-50189-x**.
8 V. N. Kitenge, D. J. Tarimo, K. O. Oyedotun, G. Rutavi and N. Manyala, Facile and sustainable technique to produce low-cost high surface area mangosteen shell activated carbon for supercapacitors applications, *J. Energy Storage*, 2022, **56**, 105876, DOI: **10.1016/j.est.2022.105876**.
9 D. J. Tarimo, K. O. Oyedotun, N. F. Sylla, A. A. Mirghni, N. M. Ndiaye and N. Manyala, Waste chicken bone-derived porous carbon materials as high performance electrode for supercapacitor applications, *J. Energy Storage*, 2022, **51**, 104378, DOI: **10.1016/j.est.2022.104378**.
10 M. Sheoran, R. Sharma, A. Dawar, S. Ojha, A. Srivastav, R. K. Sharma and O. P. Sinha, Nickel sulfide and potato-peel-derived carbon spheres composite for high-performance asymmetric supercapacitor electrodes, *J. Energy Storage*, 2024, **6**, 660, DOI: **10.1002/est2.660**.
11 F. Poli, D. Momodu, G. E. Spina, A. Terella, B. K. Mutuma, M. L. Focarete, N. Manyala and F. Soavi, Pullulan-ionic liquid-based supercapacitor: A novel, smart combination of components for an easy-to-dispose device, *Electrochim. Acta*, 2020, **338**, 135872, DOI: **10.1016/j.electacta.2020.135872**.
12 O. Fasakin, K. O. Oyedotun, A. A. Mirghni, N. F. Sylla, B. A. Mahmoud and N. Manyala, Synthesis and characterization of activated carbon derived from agricultural waste (cocoa pod husks) as potential electrode for symmetric supercapacitor, *Mater. Today Sustain.*, 2024, **28**, 101028, DOI: **10.1016/j.mtsust.2024.101028**.
13 P. Manasa, S. Sambasivam and F. Ran, Recent progress on biomass waste derived activated carbon electrode materials for supercapacitors applications—A review, *J. Energy Storage*, 2022, **54**, 1052920, DOI: **10.1016/j.est.2022.105290**.
14 X. Deng, B. Zhao, L. Zhu and Z. Shao, Molten salt synthesis of nitrogen-doped carbon with hierarchical pore structures for use as high-performance electrodes in supercapacitors, *Carbon*, 2015, **93**, 48–58, DOI: **10.1016/j.carbon.2015.05.031**.
15 Q. Abbas, R. Raza, I. Shabbir and A. G. Olabi, Heteroatom doped high porosity carbon nanomaterials as electrodes for energy storage in electrochemical capacitors: A review, *J. Sci.:Adv. Mater. Dev.*, 2019, **4**, 341–352, DOI: **10.1016/j.jsamd.2019.07.007**.
16 J. Chen, H. Wei, H. Chen, W. Yao, H. Lin and S. Han, N/P co-doped hierarchical porous carbon materials for superior performance supercapacitors, *Electrochim. Acta*, 2018, **271**, 49–57, DOI: **10.1016/j.electacta.2018.03.129**.
17 J. Shen, C. Yang, X. Li and G. Wang, High-performance asymmetric supercapacitor based on nanoarchitectured polyaniline/graphene/carbon nanotube and activated graphene electrodes, *ACS Appl. Mater. Interfaces*, 2013, **5**, 8467–8476, DOI: **10.1021/am4028235**.
18 L. Ma, J. Liu, S. Lv, Q. Zhou, X. Shen, S. Mo and H. Tong, Scalable one-step synthesis of N,S co-doped graphene-enhanced hierarchical porous carbon foam for high-performance solid-state supercapacitors, *J. Mater. Chem. A*, 2019, **7**, 7591–7603, DOI: **10.1039/C9TA00038K**.

19 V. N. Kitenge, D. J. Tarimo, K. O. Oyedotun, G. Rutavi, D. T. Bakhoum and N. Manyala, Electrical Double-Layer Capacitor Based on Low Aqueous Electrolyte Contents in EmimTFO Ionic Liquid, *Int. J. Energy Res.*, 2023, 8659009, DOI: 10.1155/2023/8659009.
20 Q. Zheng, X. Li, Q. Yang, C. Li, G. Liu, Y. Wang, P. Sun, H. Tian, C. Wang, X. Chen and J. Shao, High performance solid-state supercapacitors based on highly conductive organogel electrolyte at low temperature, *J. Power Sources*, 2022, **524**, 231102, DOI: 10.1016/j.jpowsour.2022.231102.
21 H. Zhang, X. Liu, H. Li, I. Hasa and S. Passerini, Challenges and Strategies for High-Energy Aqueous Electrolyte Rechargeable Batteries, *Angew. Chem., Int. Ed.*, 2021, **60**, 598–616, DOI: 10.1002/anie.202004433.
22 M. Saha, A. Kumar, R. Kanaoujiya, K. Behera and S. Trivedi, A Comprehensive Review of Novel Emerging Electrolytes for Supercapacitors: Aqueous and Organic Electrolytes Versus Ionic Liquid-Based Electrolytes, *Energy Fuels*, 2024, 8528–8552, DOI: 10.1021/acs.energyfuels.4c00685.
23 W. Dong, M. Xie, S. Zhao, Q. Qin and F. Huang, Materials design and preparation for high energy density and high power density electrochemical supercapacitors, *Mater. Sci. Eng., R*, 2023, **152**, 100713, DOI: 10.1016/j.mser.2022.100713.
24 L. Suo, O. Borodin, T. Gao, M. Olguin, J. Ho, X. Fan, C. Luo, C. Wang and K. Xu, "Water-in-salt" electrolyte enables high-voltage aqueous lithium-ion chemistries, n.d. https://www.science.org.
25 X. Bu, L. Su, Q. Dou, S. Lei and X. Yan, A low-cost "water-in-salt" electrolyte for a 2.3 V high-rate carbon-based supercapacitor, *J. Mater. Chem. A*, 2019, **7**, 7541–7547, DOI: 10.1039/c9ta00154a.
26 S. Lindberg, N. M. Ndiaye, N. Manyala, P. Johansson and A. Matic, A VO2 based hybrid super-capacitor utilizing a highly concentrated aqueous electrolyte for increased potential window and capacity, *Electrochim. Acta*, 2020, **345**, 136225, DOI: 10.1016/j.electacta.2020.136225.
27 G. Hasegawa, K. Kanamori, T. Kiyomura, H. Kurata, T. Abe and K. Nakanishi, Hierarchically Porous Carbon Monoliths Comprising Ordered Mesoporous Nanorod Assemblies for High-Voltage Aqueous Supercapacitors, *Chem. Mater.*, 2016, **28**, 3944–3950, DOI: 10.1021/acs.chemmater.6b01261.
28 D. Reber, R. S. Kühnel and C. Battaglia, High-voltage aqueous supercapacitors based on NaTFSI, *Sustainable Energy Fuels*, 2017, **1**, 2155–2161, DOI: 10.1039/c7se00423k.
29 V. N. Kitenge, D. J. Tarimo, K. O. Oyedotun, G. Rutavi and N. Manyala, Facile and sustainable technique to produce low-cost high surface area mangosteen shell activated carbon for supercapacitors applications, *J. Energy Storage*, 2022, **56**, 105876, DOI: 10.1016/j.est.2022.105876.
30 V. N. Kitenge, D. J. Tarimo, G. Rutavi, V. M. Maphiri, S. Sarr, M. Diop, M. Chaker and N. Manyala, Influence of nitrogen and sulfur co-doped activated carbon used as electrode material in EmiFSI ionic liquid toward high-energy supercapacitors, *J. Energy Storage*, 2024, **81**, 110453, DOI: 10.1016/j.est.2024.110453.
31 P. Dubey, P. H. Maheshwari, V. Shrivastav and S. Sundriyal, Effect of nitrogen and sulphur co-doping on the surface and diffusion characteristics of date seed-derived porous carbon for asymmetric supercapacitors, *J. Energy Storage*, 2023, **58**, 106441, DOI: 10.1016/j.est.2022.106441.
32 J. Yang, J. Peng, Y. Tang, P. Liu, Y. Lei, J. Zeng, C. Yi, Y. Shen, L. Zheng and X. Wang, Supercapacitive behaviors of N/S co-doped biomass porous carbon-based supercapacitors in "water-in-salt" electrolyte, *J. Energy Storage*, 2024, **101**, 113914, DOI: 10.1016/j.est.2024.113914.
33 X. Qian, L. Miao, J. Jiang, G. Ping, W. Xiong, Y. Lv, Y. Liu, L. Gan, D. Zhu and M. Liu, Hydrangea-like N/O codoped porous carbons for high-energy supercapacitors, *Chem. Eng. J.*, 2020, **388**, 124208, DOI: 10.1016/j.cej.2020.124208.
34 D. J. Tarimo, A. A. Mirghni, K. O. Oyedotun, G. Rutavi, V. N. Kitenge and N. Manyala, Recycling of biomass wastes from amarula husk by a modified facile economical water salt method for high energy density ultracapacitor application, *J. Energy Storage*, 2022, **53**, 105166, DOI: 10.1016/j.est.2022.105166.
35 J.-H. Choi, H. Lee, H. R. Choi and M. Cho, Graph Theory and Ion and Molecular Aggregation in Aqueous Solutions, *Annu. Rev. Phys. Chem.*, 2018, 125–149, DOI: 10.1146/annurev-physchem.
36 M. Chen, G. Feng and R. Qiao, Water-in-salt electrolytes: An interfacial perspective, *Curr. Opin. Colloid Interface Sci.*, 2020, **47**, 99–110, DOI: 10.1016/j.cocis.2019.12.011.
37 S. Han, Anionic effects on the structure and dynamics of water in superconcentrated aqueous electrolytes, *RSC Adv.*, 2019, **9**, 609–619, DOI: 10.1039/c8ra09589b.
38 L. Ji, B. Wang, Y. Yu, N. Wang and J. Zhao, N, S co-doped biomass derived carbon with sheet-like microstructures for supercapacitors, *Electrochim. Acta*, 2020, **331**, 135348, DOI: 10.1016/j.electacta.2019.135348.
39 L. Ma, J. Liu, S. Lv, Q. Zhou, X. Shen, S. Mo and H. Tong, Scalable one-step synthesis of N,S co-doped graphene-enhanced hierarchical porous carbon foam for high-performance solid-state supercapacitors, *J. Mater. Chem. A*, 2019, **7**, 7591–7603, DOI: 10.1039/C9TA00038K.
40 Z. Song, H. Duan, D. Zhu, Y. Lv, W. Xiong, T. Cao, L. Li, M. Liu and L. Gan, Ternary-doped carbon electrodes for advanced aqueous solid-state supercapacitors based on a "water-in-salt" gel electrolyte, *J. Mater. Chem. A*, 2019, **7**, 15801–15811, DOI: 10.1039/c9ta02690h.
41 D. Zhang, L. Zheng, Y. Ma, L. Lei, Q. Li, Y. Li, H. Luo, H. Feng and Y. Hao, Synthesis of nitrogen- and sulfur-codoped 3D cubic-ordered mesoporous carbon with superior performance in supercapacitors, *ACS Appl. Mater. Interfaces*, 2014, **6**, 2657–2665, DOI: 10.1021/am405128j.
42 J. Cheng, R. Jiao and Q. Sun, Free-standing N, S co-doped graphene aerogels coupled with Eucalyptus wood tar-based activated carbon and cellulose nanofibers for high-performance supercapacitor and removal of Cr(VI, *Int. J. Biol. Macromol.*, 2024, **254**, 127542, DOI: 10.1016/j.ijbiomac.2023.127542.
43 L. Sun, H. Zhou, L. Li, Y. Yao, H. Qu, C. Zhang, S. Liu and Y. Zhou, Double Soft-Template Synthesis of Nitrogen/Sulfur-Codoped Hierarchically Porous Carbon Materials Derived

from Protic Ionic Liquid for Supercapacitor, *ACS Appl. Mater. Interfaces*, 2017, **9**, 26088–26095, DOI: **10.1021/acsami.7b07877**.

44 A. Alabadi, X. Yang, Z. Dong, Z. Li and B. Tan, Nitrogen-doped activated carbons derived from a co-polymer for high supercapacitor performance, *J. Mater. Chem. A*, 2014, **2**, 11697–11705, DOI: **10.1039/c4ta01215a**.

45 S. Yaglikci, Y. Gokce, E. Yagmur and Z. Aktas, The performance of sulphur doped activated carbon supercapacitors prepared from waste tea, *Environ. Technol.*, 2020, **41**, 36–48, DOI: **10.1080/09593330.2019.1575480**.

46 K. Ning, G. Zhao, H. Liu, M. Hu, F. Huang, H. Li, L. Zhang, G. Zhu, H. Wang and J. Shi, N and S co-doped 3D hierarchical porous carbon as high-performance electrode material for supercapacitors, *Diamond Relat. Mater.*, 2022, **126**, 109080, DOI: **10.1016/j.diamond.2022.109080**.

47 Y. Shao, M. F. El-Kady, J. Sun, Y. Li, Q. Zhang, M. Zhu, H. Wang, B. Dunn and R. B. Kaner, Design and Mechanisms of Asymmetric Supercapacitors, *Chem. Rev.*, 2018, **118**, 9233–9280, DOI: **10.1021/acs.chemrev.8b00252**.

48 F. Liu, J. Niu, X. Chuan and Y. Zhao, Nitrogen and sulfur co-doping carbon in different dimensions as electrode for supercapacitor applications, *J. Alloys Compd.*, 2023, **947**, 169654, DOI: **10.1016/j.jallcom.2023.169654**.

49 G. Xin, M. M. Wang, W. Zhang, J. Song and B. Zhang, Preparation of high-capacitance N,S co-doped carbon nanospheres with hierarchical pores as supercapacitors, *Electrochim. Acta*, 2018, **291**, 168–176, DOI: **10.1016/j.electacta.2018.08.137**.

50 V. M. Maphiri, D. T. Bakhoum, S. Sarr, N. F. Sylla, G. Rutavi and N. Manyala, Low temperature thermally reduced graphene oxide directly on Ni-Foam using atmospheric pressure-chemical vapour deposition for high performance supercapacitor application, *J. Energy Storage*, 2022, **52**, 104967.

51 X. Bu, L. Su, Q. Dou, S. Lei and X. Yan, A low-cost "water-in-salt" electrolyte for a 2.3 V high-rate carbon-based supercapacitor, *J. Mater. Chem. A*, 2019, **7**, 7541–7547, DOI: **10.1039/c9ta00154a**.

52 G. Hasegawa, K. Kanamori, T. Kiyomura, H. Kurata, T. Abe and K. Nakanishi, Hierarchically Porous Carbon Monoliths Comprising Ordered Mesoporous Nanorod Assemblies for High-Voltage Aqueous Supercapacitors, *Chem. Mater.*, 2016, **28**, 3944–3950, DOI: **10.1021/acs.chemmater.6b01261**.

53 J. Yang, J. Peng, Y. Tang, P. Liu, Y. Lei, J. Zeng, C. Yi, Y. Shen, L. Zheng and X. Wang, Supercapacitive behaviors of N/S co-doped biomass porous carbon-based supercapacitors in "water-in-salt" electrolyte, *J. Energy Storage*, 2024, **101**, 113914, DOI: **10.1016/j.est.2024.113914**.

54 C. Karaman, O. Karaman, N. Atar and M. L. Yola, Sustainable electrode material for high-energy supercapacitor: Biomass-derived graphene-like porous carbon with three-dimensional hierarchically ordered ion highways, *Phys. Chem. Chem. Phys.*, 2021, **23**, 12807–12821, DOI: **10.1039/d1cp01726h**.

55 P. Lannelongue, R. Bouchal, E. Mourad, C. Bodin, M. Olarte, S. le Vot, F. Favier and O. Fontaine, "Water-in-Salt" for Supercapacitors: A Compromise between Voltage, Power Density, Energy Density and Stability, *J. Electrochem. Soc.*, 2018, **165**, A657–A663, DOI: **10.1149/2.0951803jes**.

56 D. Reber, R. S. Kühnel and C. Battaglia, High-voltage aqueous supercapacitors based on NaTFSI, *Sustainable Energy Fuels*, 2017, **1**, 2155–2161, DOI: **10.1039/c7se00423k**.

57 J. Guo, Y. Ma, K. Zhao, Y. Wang, B. Yang, J. Cui and X. Yan, High-Performance and Ultra-Stable Aqueous Supercapacitors Based on a Green and Low-Cost Water-In-Salt Electrolyte, *ChemElectroChem*, 2019, **6**, 5433–5438, DOI: **10.1002/celc.201901591**.

